https://doi.org/10.5194/npg-2024-17
Preprint. Discussion started: 24 July 2024

Nonlinear Processes in Geophysics
Discussions

Simulation characteristics of seismic translation and rotation under the assumption of nonlinear small deformation

Wei Li [1,2], Yun Wang [1,2,*], Chang Chen[1,2], Lixia Sun[1,3]

[1] *"MWMC" group, School of Geophysics and Information Technology, China University of Geosciences, Beijing* 100083*, China*

[2] *State Key Laboratory of Geological Processes and Mineral Resources, China University of Geosciences, Beijing* 100083*, China*

[3] *Sinopec Research Institute of Petroleum Engineering Co., Ltd., Beijing* 102206*, China*

[*] Corresponding author: wangyun@mail.gyig.ac.cn.

Abstract The conventional theory of elastic-wave propagation is based on classical elastodynamics, assuming linear small deformations of particles. However, recent observations of seismic rotation have revealed significant disparities between actual rotational motions induced by earthquakes in focal areas and near fields compared to theoretical calculations and simulations. Considering the nonlinearity may be the main cause of the discrepancies and based on classical elastodynamic principle, we derive seismic elastic-wave equations with Green strain tensor without the linear small deformation assumption, a different way from using complex nonlinear constitutive relation and try to interpret the mechanism of seismic rotation. By simulating and analyzing translational and rotational components subjected to the three basic and typical vibrating sources, namely, isotropic (ISO), double couple (DC),

https://doi.org/10.5194/npg-2024-17
Preprint. Discussion started: 24 July 2024

and compensated linear vector dipole (CLVD), represented by moment tensors, we investigate the wavefield differences between elastic-wave equations based on linear and nonlinear geometric relations and quantify the differences in homogeneous elastic full-space model. Subsequently, we simulate two observed six-component Taiwan earthquakes and compare their differences caused by nonlinear simulations. The results indicate that linear approximation errors are more pronounced in seismic ISO and CLVD sources. And the nonlinearity of small deformation has a more pronounced effect on rotational motions deduced by strong earthquakes. Also, the nonlinear mechanics of seismic rotation can attribute to the complex propagation paths and source mechanisms simultaneously.

https://doi.org/10.5194/npg-2024-17
Preprint. Discussion started: 24 July 2024

Nonlinear Processes in Geophysics
Discussions

1 Introduction

Seismic rotational motions are recorded in plenty of earthquakes, especially in strong shocks (Grayzer, 1991; Graizer, 2010; Zhou et al., 2019). Several studies have concluded that rotational motions cannot be neglected in shallow foci and near-field seismology (Kozak, 2009; Sun et al., 2017). In architecture engineering, rotational torsions are encouraged to be considered in assessing the stability of ground motions and building design (Li, 1991; Li and Sun, 2001; Yan, 2017; Huras et al., 2021). Many studies suggest that including seismic rotation data, which records spatial gradients, will enhance the precision of earthquake source prediction and moment tensor inversion (Bernauer et al., 2014; Donner, 2016; Ichinose et al., 2021), as validated in simulations by Hua and Zhang (2002).

Lee (2007) ever summarized the practical applications of observing seismic rotations in engineering, attributing seismic rotation to nonlinear elasticity and site effects. Notably, observed rotations during strong ground motions exceed calculated translational components by one to two orders of magnitude. Recognizing the pivotal role of nonlinear wave propagation in addressing geophysical complexities stemming from Earth's heterogeneities, various analytical solutions of nonlinear wave equations have been advanced through iterative techniques based on Green's function (McCall, 1994), including the flux-corrected transport method (Yang et al., 2002; Zheng et al., 2006), and perturbation approaches (Bataille and Contreras, 2009; Jia et al., 2020) to investigate the nonlinear effects on elastic waves. However, existing studies predominantly concentrate on the nonlinear constitutive relations of stress and strain,

https://doi.org/10.5194/npg-2024-17
Preprint. Discussion started: 24 July 2024

traditionally assuming linear small deformations (Renaud et al., 2012; Renaud et al., 2013b; TenCate et al., 2016; Feng et al., 2018), scarcely exploring nonlinearity in geometric relationship, which may be a crucial aspect that could better approximate strong rotational motions and near-field seismic conditions.

Taiwan, located in an active seismic region where earthquakes have garnered attention for their special rotational characteristics of distinctive strike-slip, particularly evident in the southern and northern areas, has been highlighted by extensive broadband seismic observations and earthquake-physical studies (Yu et al., 1999; Wang and Lv, 2006). Oliveira and Bolt's studies (1989) underscore the significant impact of rotation in near-field observations on the island, and Chen et al. (2014) discovered vertical rotations and frequency spectrum variations between horizontal and vertical rotations in the near zone of earthquakes from 2007 to 2008. These findings incline the importance of rotational studies in unraveling Taiwan's underground structures and geodynamics.

In this study, we first investigate the rotational characteristics under the assumption of nonlinear small deformation through numerical simulations of three basic seismic moment tensor sources. Additionally, we engage in theoretical simulations of six-component (6C) wavefields using observations from near and strong seismicity in Taiwan. We employ the Green strain tensor in the simulations of seismic wavefields to discuss the linear approximation and the earthquake mechanisms at play in this region.

2 Theories

https://doi.org/10.5194/npg-2024-17
Preprint. Discussion started: 24 July 2024

Nonlinear Processes in Geophysics
Discussions
Open Access

2.1 Elastodynamic theory

In a three-dimensional orthogonal Cartesian coordinate system depicting an elastic body within an elastic space, illustrated in Fig. 1, consider point **A** within the elastic body, denoted as **x**, while point **B**, located in the immediate vicinity of **A**, is indicated as **x**+d**x**. The infinitesimal distance between **A** and **B** is defined as *ds*. Under instantaneous motivation of an external force, the elastic mass element **AB** experiences displacement ***u***(***x***, t), transitioning to a new position **A'B'**, followed by small deformation of the elastic body, where the positions **A'** and **B'** are designated as ***x′*** and ***x′***+d***x′***, respectively, and their distance denoted as d***s′***. The work done by the external force is primarily transformed into kinetic energy due to displacement and potential energy stemming from elastic deformation. Hence, the change in square of the length of a line element before and after its deformation is used to measure the deformation, i.e., the squared difference in distance between **AB** and **A'B'**, expressed by Eq. (1). The following equations and tensors are written using the Kronecker symbol and dummy indicator rules.

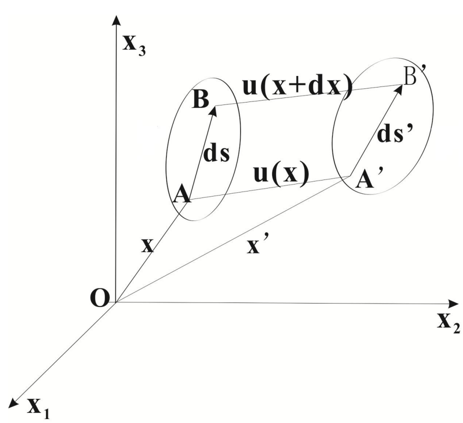

Figure 1. Schematic diagram of displacement and deformation of an elastomer

(Adapted from Aki and Richards (2002))

$$(ds')^2\text{-}(ds)^2 = (\frac{\partial u_j}{\partial x_i} + \frac{\partial u_i}{\partial x_j} + \frac{\partial u_k}{\partial x_i} \cdot \frac{\partial u_k}{\partial x_j})dx_i dx_j \text{, i, j=x, y, z} \tag{1}$$

Where u_i and u_j denote the displacements in different directions, and x_i and x_j denote the specific X, Y, and Z axes in Cartesian coordinates. Eq. (2), known as the Green strain tensor, serves as an objective measure of the strain tensor before and after the deformation of an elastomer.

$$E_{ij} = \frac{1}{2}(\frac{\partial u_j}{\partial x_i} + \frac{\partial u_i}{\partial x_j} + \frac{\partial u_k}{\partial x_i} \cdot \frac{\partial u_k}{\partial x_j}) \tag{2}$$

The strain ($\boldsymbol{e}_{ij}$) and rotation ($\boldsymbol{r}_{ij}$) tensors in elastodynamic theory are defined as:

$$e_{ji} = \frac{1}{2}(\frac{\partial u_j}{\partial x_i} + \frac{\partial u_i}{\partial x_j}) \tag{3}$$

$$r_{ji} = \frac{1}{2}(\frac{\partial u_i}{\partial x_j} - \frac{\partial u_j}{\partial x_i}) \tag{4}$$

Then, the Green strain tensor can be written as Eq. (5).

$$E_{ij} = e_{ij} + \frac{1}{2}e_{ij}^2 + \frac{1}{2}\left(e_{ij}r_{ij} - r_{ij}e_{ij}\right) - \frac{1}{2}r_{ij}^2 \tag{5}$$

The second-order displacement of nonlinearity in the Green tensor is neglected in the classical theory of kinetic elasticity. Instead, it focuses solely on the first-order linear terms, simplifying the nonlinear strain tensor to e_{ij}.

In small deformation assumption, the volumetric strain due to shear strain during elastomer deformation is overlooked, shifting the focus solely to the volumetric strain along the three principal stress axes (Eq. (6)).

$$\begin{aligned}\theta &= \frac{(1+\theta_{xx})(1+\theta_{yy})(1+\theta_{zz})dxdydz - 1dxdydz}{dxdydz} \\ &= e_{xx} + e_{yy} + e_{zz} + e_{xx}e_{yy} + e_{xx}e_{zz} + e_{yy}e_{zz} + e_{xx}e_{yy}e_{zz}\end{aligned} \tag{6}$$

https://doi.org/10.5194/npg-2024-17
Preprint. Discussion started: 24 July 2024

The simplified linear strain tensor e_{ij}, which ignores the actual nonlinear displacement term in the Green strain tensor, retains only first-order linear terms in its volumetric strain (Eq. (7)).

$$\theta_e \approx e_{xx} + e_{yy} + e_{zz} = \frac{\partial u_x}{\partial x} + \frac{\partial u_y}{\partial y} + \frac{\partial u_z}{\partial z} \tag{7}$$

The linear strain tensor, e_{ij}, disregards the nonlinearity present in the Green strain tensor, and it becomes evident that only the first-order linear terms are retained in the volumetric strain (Eq. (7)). The volumetric strain related to the Green strain tensor features nonlinear second-order displacement terms while discounting higher-order components (Eq. (8)).

$$\begin{aligned}\theta_E \approx\; & E_{xx} + E_{yy} + E_{zz} + E_{xx}E_{yy} + E_{xx}E_{zz} + E_{zz}E_{yy} \approx \frac{\partial u_x}{\partial x} + \frac{\partial u_y}{\partial y} + \frac{\partial u_z}{\partial z} + \frac{\partial u_x}{\partial x}\frac{\partial u_y}{\partial y} + \frac{\partial u_x}{\partial x}\frac{\partial u_z}{\partial z} + \frac{\partial u_y}{\partial y}\frac{\partial u_z}{\partial z} \\ & + \frac{1}{2}\left(\frac{\partial u_x}{\partial x}\cdot\frac{\partial u_x}{\partial x} + \frac{\partial u_y}{\partial x}\cdot\frac{\partial u_y}{\partial x} + \frac{\partial u_z}{\partial x}\cdot\frac{\partial u_z}{\partial x} + \frac{\partial u_x}{\partial y}\cdot\frac{\partial u_x}{\partial y} + \frac{\partial u_y}{\partial y}\cdot\frac{\partial u_y}{\partial y} + \frac{\partial u_z}{\partial y}\cdot\frac{\partial u_z}{\partial y} + \frac{\partial u_x}{\partial z}\cdot\frac{\partial u_x}{\partial z} + \frac{\partial u_y}{\partial z}\cdot\frac{\partial u_y}{\partial z} + \frac{\partial u_z}{\partial z}\cdot\frac{\partial u_z}{\partial z} \right)\end{aligned} \tag{8}$$

By combining e_{ij}, called the geometric equation, with the linear elastic constitutive equation given by Hooke and Cauchy equations, the conventional elastic-wave Navier equation (Eq. (9)) is obtained, which represents the linear elastic-wave equation within the realm of isotropic media, premised on the assumption of linear small deformations.

$$\rho \frac{\partial^2 u_i}{\partial t^2} = \rho f_i + (\lambda + \mu)\frac{\partial \theta}{\partial x_i} + \mu \frac{\partial^2 u_i}{\partial x_j \partial x_j} \tag{9}$$

Where ρ symbolizes the density, t denotes the time, f_i denotes the body force, and λ alongside μ represents the Lamé coefficients. In the nonlinear small deformation scenario, substituting the Green strain tensor and its corresponding volumetric strain into constitutive equation and equations of motion, culminating in the formulation of

https://doi.org/10.5194/npg-2024-17
Preprint. Discussion started: 24 July 2024

Nonlinear Processes in Geophysics
Discussions

the subsequent equation:

$$\begin{aligned}\rho\frac{\partial^2 u_i}{\partial t^2} &= \rho f_i + (\lambda+\mu)\frac{\partial\theta}{\partial x_i} + \mu\frac{\partial^2 u_i}{\partial x_j\partial x_j}\\ &+\lambda\left[\frac{\partial^2 u_k}{\partial x_i x_j}\cdot\frac{\partial u_k}{\partial x_j} + \frac{\partial}{\partial x_i}\left(\frac{\partial u_x}{\partial x_x}\cdot\frac{\partial u_y}{\partial x_y} + \frac{\partial u_x}{\partial x_x}\cdot\frac{\partial u_z}{\partial x_z} + \frac{\partial u_y}{\partial x_y}\cdot\frac{\partial u_z}{\partial x_z}\right)\right] + \mu\left(\frac{\partial^2 u_k}{\partial x_i x_j}\cdot\frac{\partial u_k}{\partial x_j} + \frac{\partial^2 u_k}{\partial x_j x_j}\cdot\frac{\partial u_k}{\partial x_i}\right)\end{aligned} \tag{10}$$

Eq. (10) introduces several third-order terms diverging from the composition of Eq. (9). Their difference unveils the nonlinearity in terms of the displacement field **u** and the elastic parameters (μ and λ) under nonlinear small deformation. Eq. (10) exhibits more complexity, signifying the introduction of additional physical intricacies into an elastomer's deformation dynamics. The inclusion of nonlinear terms describes the nonlinear response of the medium by linking it with the shear modulus (μ) and the bulk modulus (λ), thereby impacting the propagation attributes of elastic waves. The increment of the equation associated with the shear modulus μ engenders nonlinear effects via the strain tensor, while the increment associated with the bulk modulus λ induces nonlinear effects through the volumetric strain.

The disparity between the two wave equations does not directly translate to the final displacement field discrepancies. The displacement field in Eq. (10) is the result of the nonlinear small deformation, in contrast to Eq. (9), where such nonlinear effects are absent. Therefore, the velocity-stress equations using the Green strain tensor are derived next to compare the difference in wave fields between the two by numerical simulation of seismic wavefields.

2.2 Velocity-stress elastic wave equations

The staggered-grid finite-difference method is well-established for performing

https://doi.org/10.5194/npg-2024-17
Preprint. Discussion started: 24 July 2024

numerical simulations of seismic wavefields. By discretizing the medium and the wave equations, the numerical solution of the wavefield is obtained at each grid point under each time node as time progresses. In general, the first-order velocity-stress elastic wave equations under the assumption of linear small deformation in 3-dimensional (3D) isotropic media are

$$
\begin{cases}
\frac{\partial \sigma_{xx}}{\partial x}+\frac{\partial \sigma_{xy}}{\partial y}+\frac{\partial \sigma_{xz}}{\partial z}+f_x=\rho\frac{\partial v_x}{\partial t}\\
\frac{\partial \sigma_{yx}}{\partial x}+\frac{\partial \sigma_{yy}}{\partial y}+\frac{\partial \sigma_{yz}}{\partial z}+f_y=\rho\frac{\partial v_y}{\partial t}\\
\frac{\partial \sigma_{zx}}{\partial x}+\frac{\partial \sigma_{zy}}{\partial y}+\frac{\partial \sigma_{zz}}{\partial z}+f_z=\rho\frac{\partial v_z}{\partial t}
\end{cases}
$$

$$
\begin{cases}
\frac{\partial \sigma_{xx}}{\partial t}=(\lambda+2\mu)\frac{\partial v_x}{\partial x}+\lambda\frac{\partial v_y}{\partial y}+\lambda\frac{\partial v_z}{\partial z}\\
\frac{\partial \sigma_{yy}}{\partial t}=\lambda\frac{\partial v_x}{\partial x}+(\lambda+2\mu)\frac{\partial v_y}{\partial y}+\lambda\frac{\partial v_z}{\partial z}\\
\frac{\partial \sigma_{zz}}{\partial t}=\lambda\frac{\partial v_x}{\partial x}+\lambda\frac{\partial v_y}{\partial y}+(\lambda+2\mu)\frac{\partial v_z}{\partial z}\\
\frac{\partial \sigma_{xy}}{\partial t}=\mu(\frac{\partial v_y}{\partial x}+\frac{\partial v_x}{\partial y})\\
\frac{\partial \sigma_{xz}}{\partial t}=\mu(\frac{\partial v_z}{\partial x}+\frac{\partial v_x}{\partial z})\\
\frac{\partial \sigma_{yz}}{\partial t}=\mu(\frac{\partial v_z}{\partial y}+\frac{\partial v_y}{\partial z})
\end{cases}
\tag{11}
$$

$$
\begin{cases}
R_x=\frac{1}{2}(\frac{\partial v_z}{\partial y}-\frac{\partial v_y}{\partial z})\\
R_y=\frac{1}{2}(\frac{\partial v_x}{\partial z}-\frac{\partial v_z}{\partial x})\\
R_z=\frac{1}{2}(\frac{\partial v_y}{\partial x}-\frac{\partial v_x}{\partial y})
\end{cases}
$$

Where $\boldsymbol{\sigma}_{ji}$ denotes the stress tensor, v_x, v_y, and v_z denote the velocity of X, Y, and Z components. $\mathbf{R}_{xz}$ corresponds to the rotation rate around Y axis, commonly referred to as $\mathbf{R}_Y$ in rotational seismology, as well as $\mathbf{R}_X$ and $\mathbf{R}_Z$.

Similarly, the velocity-stress elastic wave equations under the assumption of nonlinear small deformation in 3D isotropic media can be given as Eq. (12).

https://doi.org/10.5194/npg-2024-17
Preprint. Discussion started: 24 July 2024

Nonlinear Processes in Geophysics
Discussions

$$
\begin{cases}
\frac{\partial \sigma_{xx}}{\partial x}+\frac{\partial \sigma_{xy}}{\partial y}+\frac{\partial \sigma_{xz}}{\partial z}+f_x=\rho\frac{\partial v_x}{\partial t}\\
\frac{\partial \sigma_{yx}}{\partial x}+\frac{\partial \sigma_{yy}}{\partial y}+\frac{\partial \sigma_{yz}}{\partial z}+f_y=\rho\frac{\partial v_y}{\partial t}\\
\frac{\partial \sigma_{zx}}{\partial x}+\frac{\partial \sigma_{zy}}{\partial y}+\frac{\partial \sigma_{zz}}{\partial z}+f_z=\rho\frac{\partial v_z}{\partial t}
\end{cases}
$$

$$
\begin{cases}
\frac{\partial \sigma_{xx}}{\partial t}=(\lambda+2\mu)\frac{\partial v_x}{\partial x}+\lambda\frac{\partial v_y}{\partial y}+\lambda\frac{\partial v_z}{\partial z}+2\,dt\cdot\lambda\cdot\left(\frac{\partial v_x}{\partial x}\frac{\partial v_y}{\partial y}+\frac{\partial v_x}{\partial x}\frac{\partial v_z}{\partial z}+\frac{\partial v_y}{\partial y}\frac{\partial v_z}{\partial z}\right)+dt\cdot(\lambda+2\mu)\cdot\left(\frac{\partial v_x}{\partial x}\frac{\partial v_x}{\partial x}+\frac{\partial v_y}{\partial x}\frac{\partial v_y}{\partial x}+\frac{\partial v_z}{\partial x}\frac{\partial v_z}{\partial x}\right)\\
+dt\cdot\lambda\cdot\left(\frac{\partial v_x}{\partial y}\frac{\partial v_x}{\partial y}+\frac{\partial v_y}{\partial y}\frac{\partial v_y}{\partial y}+\frac{\partial v_z}{\partial y}\frac{\partial v_z}{\partial y}\right)+dt\cdot\lambda\cdot\left(\frac{\partial v_x}{\partial z}\frac{\partial v_x}{\partial z}+\frac{\partial v_y}{\partial z}\frac{\partial v_y}{\partial z}+\frac{\partial v_z}{\partial z}\frac{\partial v_z}{\partial z}\right)\\
\frac{\partial \sigma_{yy}}{\partial t}=\lambda\frac{\partial v_x}{\partial x}+(\lambda+2\mu)\frac{\partial v_y}{\partial y}+\lambda\frac{\partial v_z}{\partial z}+2\,dt\cdot\lambda\cdot\left(\frac{\partial v_x}{\partial x}\frac{\partial v_y}{\partial y}+\frac{\partial v_x}{\partial x}\frac{\partial v_z}{\partial z}+\frac{\partial v_y}{\partial y}\frac{\partial v_z}{\partial z}\right)+dt\cdot\lambda\cdot\left(\frac{\partial v_x}{\partial x}\frac{\partial v_x}{\partial x}+\frac{\partial v_y}{\partial x}\frac{\partial v_y}{\partial x}+\frac{\partial v_z}{\partial x}\frac{\partial v_z}{\partial x}\right)\\
+dt\cdot(\lambda+2\mu)\cdot\left(\frac{\partial v_x}{\partial y}\frac{\partial v_x}{\partial y}+\frac{\partial v_y}{\partial y}\frac{\partial v_y}{\partial y}+\frac{\partial v_z}{\partial y}\frac{\partial v_z}{\partial y}\right)+dt\cdot\lambda\cdot\left(\frac{\partial v_x}{\partial z}\frac{\partial v_x}{\partial z}+\frac{\partial v_y}{\partial z}\frac{\partial v_y}{\partial z}+\frac{\partial v_z}{\partial z}\frac{\partial v_z}{\partial z}\right)\\
\frac{\partial \sigma_{zz}}{\partial t}=\lambda\frac{\partial v_x}{\partial x}+\lambda\frac{\partial v_y}{\partial y}+(\lambda+2\mu)\frac{\partial v_z}{\partial z}+2\,dt\cdot\lambda\cdot\left(\frac{\partial v_x}{\partial x}\frac{\partial v_y}{\partial y}+\frac{\partial v_x}{\partial x}\frac{\partial v_z}{\partial z}+\frac{\partial v_y}{\partial y}\frac{\partial v_z}{\partial z}\right)+dt\cdot\lambda\cdot\left(\frac{\partial v_x}{\partial x}\frac{\partial v_x}{\partial x}+\frac{\partial v_y}{\partial x}\frac{\partial v_y}{\partial x}+\frac{\partial v_z}{\partial x}\frac{\partial v_z}{\partial x}\right)\\
+dt\cdot\lambda\cdot\left(\frac{\partial v_x}{\partial y}\frac{\partial v_x}{\partial y}+\frac{\partial v_y}{\partial y}\frac{\partial v_y}{\partial y}+\frac{\partial v_z}{\partial y}\frac{\partial v_z}{\partial y}\right)+dt\cdot(\lambda+2\mu)\cdot\left(\frac{\partial v_x}{\partial z}\frac{\partial v_x}{\partial z}+\frac{\partial v_y}{\partial z}\frac{\partial v_y}{\partial z}+\frac{\partial v_z}{\partial z}\frac{\partial v_z}{\partial z}\right)\\
\frac{\partial \sigma_{xy}}{\partial t}=\mu\left(\frac{\partial v_y}{\partial x}+\frac{\partial v_x}{\partial y}\right)+dt\cdot 2\mu\cdot\left(\frac{\partial v_x}{\partial x}\frac{\partial v_x}{\partial y}+\frac{\partial v_y}{\partial x}\frac{\partial v_y}{\partial y}+\frac{\partial v_z}{\partial x}\frac{\partial v_z}{\partial y}\right)\\
\frac{\partial \sigma_{xz}}{\partial t}=\mu\left(\frac{\partial v_x}{\partial z}+\frac{\partial v_z}{\partial x}\right)+dt\cdot 2\mu\cdot\left(\frac{\partial v_x}{\partial z}\frac{\partial v_x}{\partial x}+\frac{\partial v_y}{\partial z}\frac{\partial v_y}{\partial x}+\frac{\partial v_z}{\partial z}\frac{\partial v_z}{\partial x}\right)\\
\frac{\partial \sigma_{yz}}{\partial t}=\mu\left(\frac{\partial v_z}{\partial y}+\frac{\partial v_y}{\partial z}\right)+dt\cdot 2\mu\cdot\left(\frac{\partial v_x}{\partial y}\frac{\partial v_x}{\partial z}+\frac{\partial v_y}{\partial y}\frac{\partial v_y}{\partial z}+\frac{\partial v_z}{\partial y}\frac{\partial v_z}{\partial z}\right)
\end{cases}
\tag{12}
$$

$$
\begin{cases}
R_x=\frac{1}{2}\left(\frac{\partial v_z}{\partial y}-\frac{\partial v_y}{\partial z}\right)\\
R_y=\frac{1}{2}\left(\frac{\partial v_x}{\partial z}-\frac{\partial v_z}{\partial x}\right)\\
R_z=\frac{1}{2}\left(\frac{\partial v_y}{\partial x}-\frac{\partial v_x}{\partial y}\right)
\end{cases}
$$

Where the variables and symbols are defined in the same way as in Eq. (11).

2.3 Staggered-grid finite difference method

This study utilizes the staggered-grid finite difference method to simulate the seismic wavefields (Sun et al., 2018). The model is divided into two sets of grids, wherein the velocity and stress of the medium are defined in separate grid systems (Madariaga, 1976). The grid configuration for a two-dimensional model scenario is illustrated in Fig. 2.

https://doi.org/10.5194/npg-2024-17
Preprint. Discussion started: 24 July 2024

Nonlinear Processes in Geophysics
Discussions

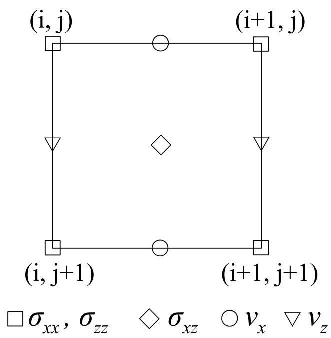

Figure 2. Schematic diagram of 2D staggered grids.

Based on Eqs. (11) and (12), we can simulate the seismic waves propagating in discrete grids with two-order time and six-order space differential approximations. To weaken the boundary reflections, perfectly matched absorbing layer boundary conditions are adapted to the boundaries (Dong & Ma 2000). Alternatively, the acoustic boundary replacement method is adopted to ensure the free-surface condition at the upper boundary (Xu et al., 2007; Wang et al., 2012).

2.4 Simulation parameters

For the physical process of source excitation, when the seismic wavelength under study substantially surpasses the scale of the involved source, the seismic source can be regarded as a point source. The seismic moment tensor, represented by equation (13), is the most comprehensive depiction of seismic point sources.

$$\boldsymbol{M} = \begin{pmatrix} M_{xx} & M_{xy} & M_{xz} \\ M_{yx} & M_{yy} & M_{yz} \\ M_{zx} & M_{zy} & M_{zz} \end{pmatrix}, i, j = x, y, z \tag{13}$$

In Eq. (11), M_{ij} represents each moment-element component. The first index signifies the force direction, and the second index signifies the direction of force arm.

https://doi.org/10.5194/npg-2024-17
Preprint. Discussion started: 24 July 2024

The moment tensor can be decomposed into three distinct parts: the isotropy component (ISO), the double couple component (DC), and the compensated linear vector dipole component (CLVD) (Knopoff and Randall, 1970). The ISO component represents the volume expansion of the focal area, characterized by a non-zero trace and uniform force and direction of force arm in three vector dipoles. The DC component denotes the dislocation of the two fault walls without volume variation. The CLVD component is also composed of three vector dipoles, with one being twice as large as the other two. The three basic seismic source components can be expressed as follows.

$$\boldsymbol{M}^{ISO}=\begin{pmatrix} M_{xx} & 0 & 0 \\ 0 & M_{yy} & 0 \\ 0 & 0 & M_{zz} \end{pmatrix} \tag{14}$$

$$\boldsymbol{M}^{DC}=\begin{pmatrix} 0 & M_{xy} & 0 \\ M_{yx} & 0 & 0 \\ 0 & 0 & 0 \end{pmatrix} \tag{15}$$

$$\boldsymbol{M}^{CLVD}=\begin{pmatrix} M_{xx} & 0 & 0 \\ 0 & M_{yy} & 0 \\ 0 & 0 & -2M_{zz} \end{pmatrix} \tag{16}$$

In numerical simulations, the Ricker wavelet with a central frequency of 0.5 Hz is employed as a seismic source wavelet to simulate the three simplest sources: ISO, DC, and CLVD. The body force, represented by the moment tensor, can be converted into a velocity source by incrementally being added to individual velocity components to simulate the three basic sources (Graves, 1996). The specific loading equations in the grid system are outlined below.

https://doi.org/10.5194/npg-2024-17
Preprint. Discussion started: 24 July 2024

Nonlinear Processes in Geophysics
Discussions
Open Access

$$\mathrm{ISO}:\begin{cases}\Delta v_x^{n+\frac{1}{2}}\left(i+\frac{1}{2},j,k\right)=\frac{M_{xx}dt}{\rho Vdx}f^n\\ \Delta v_x^{n+\frac{1}{2}}\left(i-\frac{1}{2},j,k\right)=\frac{-M_{xx}dt}{\rho Vdx}f^n\\ \Delta v_y^{n+\frac{1}{2}}\left(i,j+\frac{1}{2},k\right)=\frac{M_{yy}dt}{\rho Vdy}f^n\\ \Delta v_y^{n+\frac{1}{2}}\left(i,j-\frac{1}{2},k\right)=\frac{-M_{yy}dt}{\rho Vdy}f^n\\ \Delta v_z^{n+\frac{1}{2}}\left(i,j,k+\frac{1}{2}\right)=\frac{M_{zz}dt}{\rho Vdz}f^n\\ \Delta v_z^{n+\frac{1}{2}}\left(i,j,k-\frac{1}{2}\right)=\frac{-M_{zz}dt}{\rho Vdz}f^n\end{cases}\tag{17}$$

$$\mathrm{DC}:\begin{cases}\Delta v_x^{n+\frac{1}{2}}\left(i+\frac{1}{2},j,k\right)=\frac{-M_{xy}dt}{\rho Vdy}f^n\\ \Delta v_x^{n+\frac{1}{2}}\left(i+\frac{1}{2},j-1,k\right)=\frac{M_{xy}dt}{\rho Vdy}f^n\\ \Delta v_y^{n+\frac{1}{2}}\left(i,j-\frac{1}{2},k\right)=\frac{M_{yx}dt}{\rho Vdx}f^n\\ \Delta v_y^{n+\frac{1}{2}}\left(i+1,j-\frac{1}{2},k\right)=\frac{-M_{yx}dt}{\rho Vdx}f^n\end{cases}\tag{18}$$

$$\mathrm{CLVD}:\begin{cases}\Delta v_x^{n+\frac{1}{2}}\left(i+\frac{1}{2},j,k\right)=\frac{M_{xx}dt}{\rho Vdx}f^n\\ \Delta v_x^{n+\frac{1}{2}}\left(i-\frac{1}{2},j,k\right)=\frac{-M_{xx}dt}{\rho Vdx}f^n\\ \Delta v_y^{n+\frac{1}{2}}\left(i,j+\frac{1}{2},k\right)=\frac{M_{yy}dt}{\rho Vdy}f^n\\ \Delta v_y^{n+\frac{1}{2}}\left(i,j-\frac{1}{2},k\right)=\frac{-M_{yy}dt}{\rho Vdy}f^n\\ \Delta v_z^{n+\frac{1}{2}}\left(i,j,k+\frac{1}{2}\right)=\frac{-2M_{zz}dt}{\rho Vdz}f^n\\ \Delta v_z^{n+\frac{1}{2}}\left(i,j,k-\frac{1}{2}\right)=\frac{2M_{zz}dt}{\rho Vdz}f^n\end{cases}\tag{19}$$

Δv denotes the velocity increment; n denotes the time sampling node; dt, ρ, and V represent the time sampling interval, medium density, and the medium model's unit volume, respectively. The source-time function f^n denotes the Ricker wavelet's amplitude at the corresponding time node.

https://doi.org/10.5194/npg-2024-17
Preprint. Discussion started: 24 July 2024

Nonlinear Processes in Geophysics
Discussions

To focus on the influence of different small deformation scenarios on seismic elastic waves, we only discuss the characteristics in a 3D isotropic full-space homogeneous medium. The model is set with a size of 60 km (x) × 60 km (y)× 60 km (z), with mesh division spacing set at 0.5 km. Model properties include v_p=4400 m/s, v_s=3000 m/s, and ρ=2600 kg/m^3. The moment source is positioned at the model's center, where x=y=z=30 km. The time sampling interval is 15 ms, and the total recording time spans 10 seconds.

3 Wavefield simulations of three types of basic seismic source

3.1 ISO source

Under the assumption of nonlinear small deformation related to the condition of the Green strain tensor, the 3-component translational and rotational seismic snapshots are synthesized and illustrated in Fig. 3a. These snapshots demonstrate the generation of solely P-wave, with minimal energy projected in rotational components upon the excitation of ISO source.

To highlight the distinction in wave propagation between linear and nonlinear conditions, we present the wavefield difference and their approximation with the relative change in Fig. 3b and c. Minimal disparities are observed in P-wave fronts, indicating that the assumption of linear small deformation is satisfied for P-wave in ISO source simulation. Conversely, examining the S-wave fronts in Fig. 3b and their relative changes (ranging approximately between 5-20 percent) in Fig. 3c lead to the

https://doi.org/10.5194/npg-2024-17
Preprint. Discussion started: 24 July 2024

Nonlinear Processes in Geophysics
Discussions
Open Access

conclusion that even in the ISO simulation, the coupling of P- and S-waves in the wave equations allows the generation of S-waves, a phenomenon that is unattainable under conditions of linear small deformation.

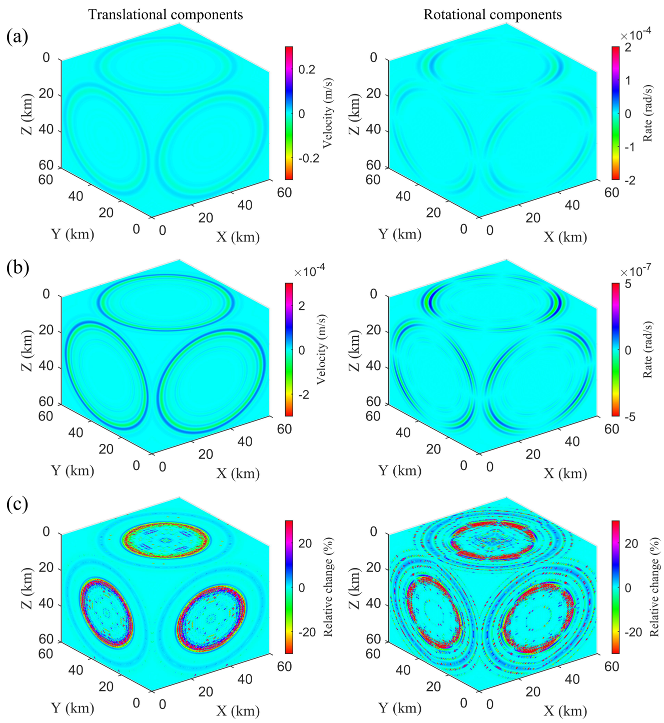

Figure 3. Wavefield comparisons at 8th second excited by ISO source. (a) presents the wavefield snapshots under nonlinear small deformation, (b) presents the difference between linear and nonlinear conditions, and (c) presents their relative change in percentage (using the linear result as the denominator)

3.2 DC source

The wavefields excited by the DC source are illustrated in Fig. 4a, revealing the generation of relatively weak P and stronger S waves. The application of double force

https://doi.org/10.5194/npg-2024-17
Preprint. Discussion started: 24 July 2024

moments (M_{xy} and M_{yx}) loaded within the x-y plane results in the X- and Y-components of translational motions being stronger than the Z-component. Consequently, the $\mathbf{R}_Z$ exhibits a greater degree of wavefield energy than the $\mathbf{R}_X$ and $\mathbf{R}_Y$ components. From the wavefield differences and relative change between the two assumptions (Fig. 4b and c), it becomes evident that the discrepancy in S-wave is notable, and the relative change in P wave is more prominent in the rotational components (below 10 %). Moreover, the distinction in the wavefront polarity of the P- and S-wave in the wavefield caused by nonlinearity is totally different from the polarity of the wavefield itself, as illustrated in Fig. 4a.

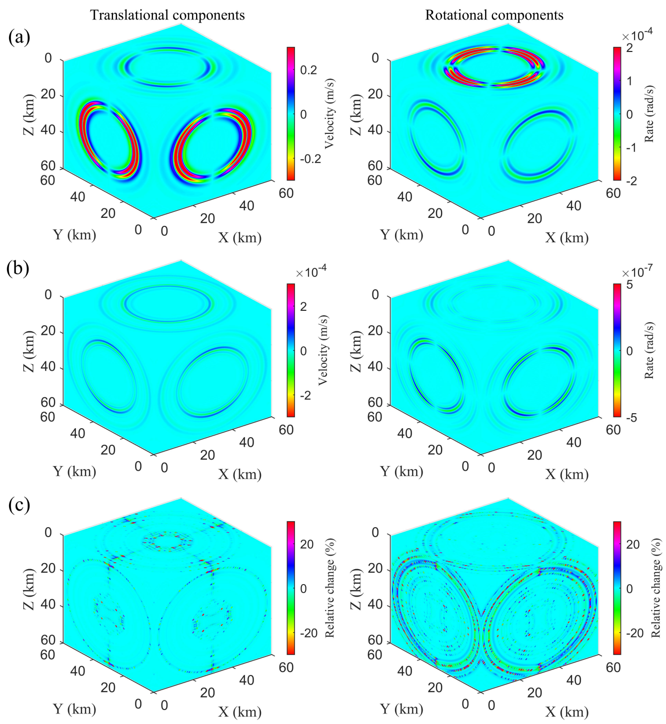

Figure 4. Wavefield comparisons at 8th second excited by DC source. (a) presents the wavefield snapshots under nonlinear small deformation, (b) presents the

https://doi.org/10.5194/npg-2024-17
Preprint. Discussion started: 24 July 2024

difference between the linear and nonlinear conditions, and (c) presents their relative change with percentage (using the linear result as the denominator)

3.3 CLVD source

Fig. 5a displays the results generated by CLVD source. In comparison to the outcomes of ISO and DC sources, the CLVD elicits more pronounced S waves primarily projected in $\mathbf{R}_X$ and $\mathbf{R}_Y$ components. Moreover, the wavefield differences between linearity and nonlinearity intensify, particularly in S wave in rotational motion (Fig. 5b). Their maximum relative change can reach up to 10 percent, especially along the diagonal direction of 45 degrees (Fig. 5c).

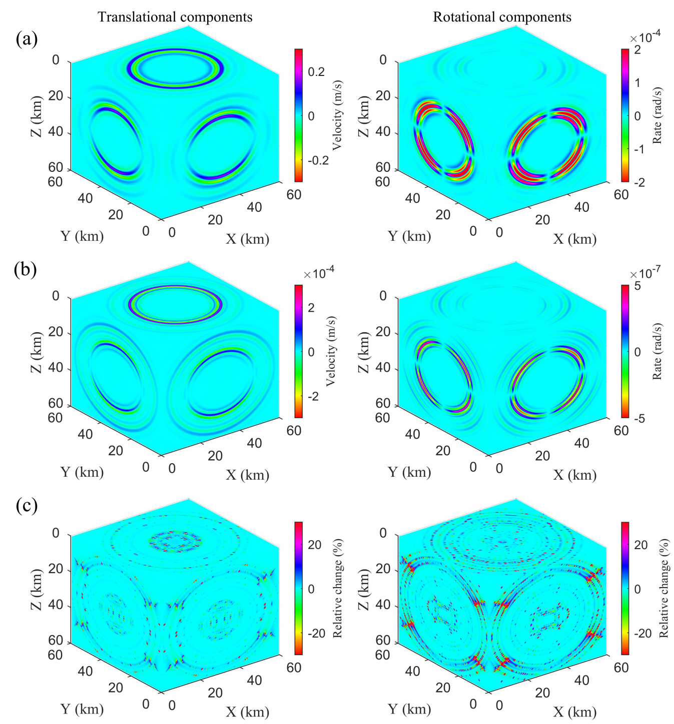

Figure 5. Wavefield comparisons at 8th second excited by CLVD source. (a)

https://doi.org/10.5194/npg-2024-17
Preprint. Discussion started: 24 July 2024

presents the wavefield snapshots under nonlinear small deformation, (b) presents the difference between the linear and nonlinear conditions, and (c) presents their relative change with percentage (using the linear result as the denominator)

3.4 Comparisons of wavefield energy for basic seismic sources

The disparities in propagation of nonlinear elastic waves in homogeneous media are predominantly observed in rotational components, as evidenced by the aforementioned comparisons and analyses. Further calculating the wavefield energy for the above wavefield snapshot display area and comparing the variations of wave energy in relative changes over time progression and the change at the 8th second with the seismic moment magnitude increasing, as illustrated in Fig. 6. In Fig. 6a, the overall errors in wavefield energy consistently remain below 1 percent as the wave propagates near the source area with small magnitude, signifying that the linear assumption is adequate for the three basic moment tensor sources. In Fig. 6b, the changing curves for the DC source display less smoothness than those for the CLVD, and the relative change in rotational components consistently outweighs this in translational components. Moreover, the curves demonstrate a nearly exponential increase with rising earthquake magnitude. Upon reaching a strong magnitude of 7, especially for the ISO source, the errors in rotational motions reach 25 percent, while these in translation amount to approximately 10 percent. The error due to CLVD sources can also reach about 5 %, while the DC-induced error remains small. Because the DC source component typically dominates the focal mechanisms for the majority

https://doi.org/10.5194/npg-2024-17
Preprint. Discussion started: 24 July 2024

of earthquakes, as opposed to the ISO component (Zhao and Zhang, 2022), it can be inferred that the approximation of linear scenario is well-suited for the majority of seismic body waves simulations, except in instances of strong seismic activity.

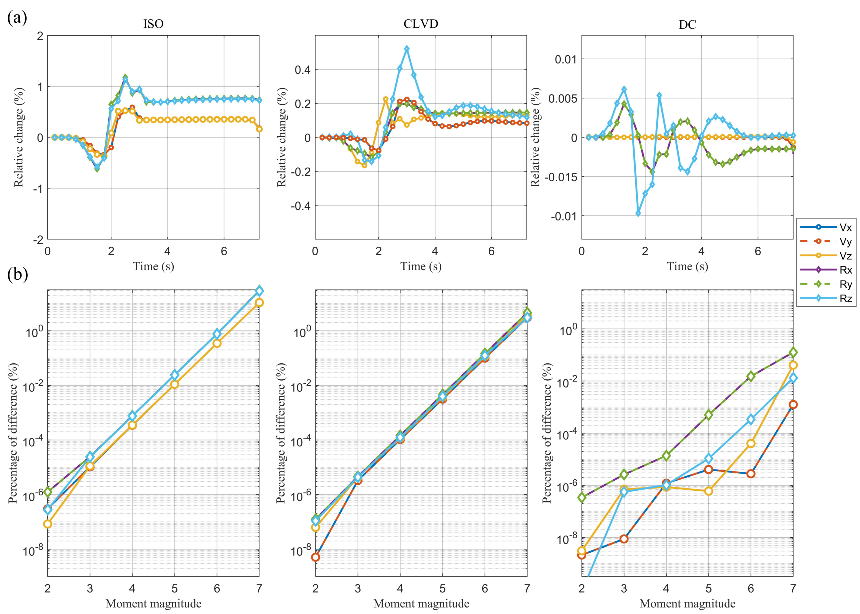

Figure 6. Relative changes of wavefield energy induced by nonlinearity with (a) spreading time and (b) increasing earthquake magnitude

4 Seismic observations and simulations of two Taiwan earthquakes

4.1 Hualien earthquakes

Taiwan, situated at the confluence of three significant tectonic plates - the Philippine Sea Plate, the Eurasia Plate, and the Pacific Ocean Plate, experiences frequent seismic activity, particularly moderate to large earthquakes annually (Zheng et al., 2005). The 2018 Hualien earthquake with a magnitude of M_W 5.41 (referred to

https://doi.org/10.5194/npg-2024-17
Preprint. Discussion started: 24 July 2024

Nonlinear Processes in Geophysics
Discussions

as **E**1) and the 2019 Hualien earthquake with a magnitude of $\boldsymbol{M_W}$ 6.13 (referred to as **E**2), with epicenter depths of 15 km and 30 km, respectively, occurred off the eastern coast of Taiwan. The epicenter locations and station placements depicted by GMT are shown in Fig. 7 (Wessel et al., 2019). The receiver for **E**2, located in Fujian province, is positioned 327 km from the epicenter (Fig. 7a). Additionally, a seismic array comprising seven 3C translational seismometers was deployed approximately 53 km from the epicenter of **E**1 (Yuan et al., 2020) (Fig. 7b). A blueSeis-3A fiber-optic rotational seismometer was placed at the NA01 station in the center of the array to directly record the seismic rotational rates (Bernauer et al. 2018; Cao et al., 2021).

According to the monitoring data from the U.S. Geological Survey (USGS, https://www.usgs.gov/), both **E**1 and **E**2 were triggered by reverse faults, and beach balls representing their focal mechanisms are shown in Fig. 7c. The moment tensor parameters of **E**1 and **E**2 are presented in Eqs. (20) and (21), respectively.

https://doi.org/10.5194/npg-2024-17
Preprint. Discussion started: 24 July 2024

Nonlinear Processes in Geophysics
Discussions
Open Access

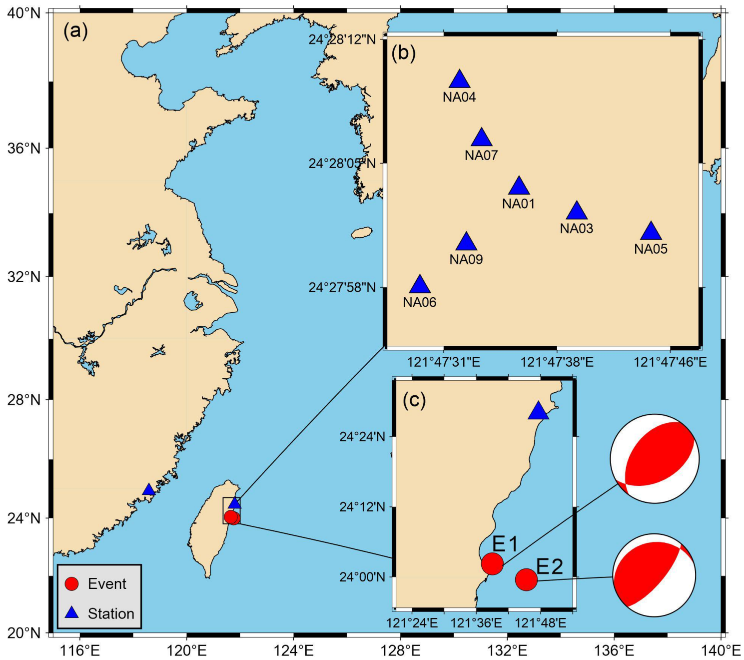

Figure 7. Epicenters and observation sites of the two earthquakes

$$\begin{aligned} M_{rr} &= 9.942\times10^{16}, M_{tt} = -7.569\times10^{16}, M_{pp} = -2.373\times10^{16} \\ M_{rt} &= 7.372\times10^{16}, M_{rp} = 1.0965\times10^{17}, M_{tp} = -4.156\times10^{16} \end{aligned} \tag{20}$$

$$\begin{aligned} M_{rr} &= 1.8247\times10^{18}, M_{tt} = -1.064\times10^{18}, M_{pp} = -7.607\times10^{17} \\ M_{rt} &= 3.141\times10^{17}, M_{rp} = -3.155\times10^{17}, M_{tp} = -1.114\times10^{18} \end{aligned} \tag{21}$$

4.2 Wavefield simulations of the Taiwan earthquakes

To simulate **E**1 and **E**2, we implement the free-surface condition at the upper surface and absorbing boundary conditions in other directions of the 3D model. According to the CRUST1.0 model (Laske et al., 2013), the subsurface medium at the **E**1 observation station is divided into five distinct layers, as detailed in Table 1. The 3D model is constructed with a size of 60 km (x, NS) × 20 km (y, EW) × 30 km (z,

https://doi.org/10.5194/npg-2024-17
Preprint. Discussion started: 24 July 2024

vertical) to suit the specifics of the observation system, with the corresponding parameters shown in Table 2.

Table 1 Underground layered medium at observing stations

Layer	Thickness (km)	Vp (km/s)	Vs (km/s)	ρ (kg/m³)
1	0.50	2.50	1.07	2.11
2	10.12	5.80	3.40	2.63
3	9.81	6.30	3.62	2.74
4	9.82	6.90	3.94	2.92
5	-	7.70	4.29	3.17

Table 2 Parameters for simulating model 1 (**E**1)

Items	Parameters
Source type	Eq. (20)
Central frequency	1 Hz
Grid interval	1 km
Time interval	5 ms
Source position	(0, 0, 15 km)
Receiver position	(53 km, : , 0 km)
Recording time	30 s

Sorting the synthetic records from model 1 at coordinates X=53 km and Y=4 km, corresponding to the NA01 station, the seismic waveforms are presented in Fig. 8a. It can be found that, apart from direct P- and S-waves, **E**1 predominantly exhibits elliptical polarization in X-Z vertical plane and rotational movements around Y-axis induced by Rayleigh wave in the north-south vertical plane. The large order of magnitude difference in amplitude between theoretical simulations and actual observations is due to the assumption of elastic media, though the actual propagation media are usually viscoelastic, which will absorb and attenuate seismic energy and high frequency.

https://doi.org/10.5194/npg-2024-17
Preprint. Discussion started: 24 July 2024

Nonlinear Processes in Geophysics
Discussions

The unavoidable site effect leads to the practical observation in Fig. 8b displaying significantly stronger horizontal components than vertical ones (Abercrombie, 1997; Guatteri et al., 2001). The site effect and the nearly northeast strike of the seismogenic fault result in pronounced translational components and $\mathbf{R}_Z$ component recordings mixed with complex seismic waves after P- and S-wave arrivals, indicating the presence of Love waves and significant disparities between the actual Earth's medium and the simplified Crust model. Fig. 8 also shows that the simulated rotational components are 1000 times of magnitude weaker than the simulated translational components, but the observed rotational motions are 250 times weaker than the translational ones.

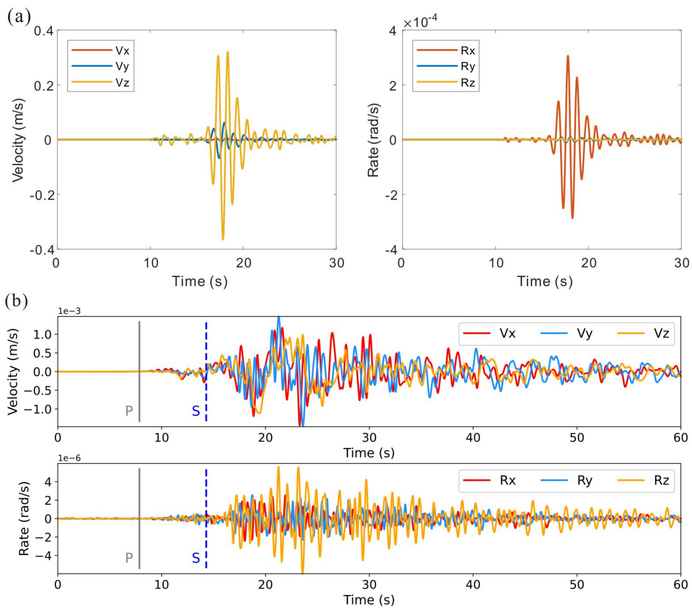

Figure 8. 6C seismic records of (a) theoretical simulation under linear small deformation for **E**1. In (b), for the real seismic records, a band-pass filter of 0.1 Hz to 2 Hz is applied, and the corresponding arrival times of P and S waves are calculated

https://doi.org/10.5194/npg-2024-17
Preprint. Discussion started: 24 July 2024

Nonlinear Processes in Geophysics
Open Access
EGU
Discussions

according to the iasp91 model (Kennett and Engdahl, 1991)

Table 3 Parameters for simulating model 2 (**E**2).

Items	Parameters
Source type	Eq. (21)
Central frequency	0.5 Hz
Grid interval	5 km
Time interval	2 ms
Source position	(0, 310 km, 30 km)
Receiver position	(:, 0 km, 0 km)
Recording time	300 s

The same modeling approach is adopted to simulate **E**2, with the parameters of model 2 detailed in Table 3, featuring a size of 150 km (x, NS) × 350 km (y, EW) × 50 km (z, vertical). The 6C seismic recordings at X=100 km and Y=0 km, corresponding to the receiver station, are extracted from the simulation result of model 2, as displayed in Fig. 9a. The simulated records show a dominance of $\mathbf{V}_Z$ over $\mathbf{V}_X$ and $\mathbf{V}_Y$ components, with $\mathbf{R}_X$ and $\mathbf{R}_Y$ components exhibiting more strength than $\mathbf{R}_Z$ component, showcasing the rotational motions primarily occurring in the horizontal direction. In addition to the direct P and S waves and surface waves, this intense seismic shock generated strong secondary waves. In the actual observation records (Fig. 9b), where the station is located on solid rock within a tunnel, the $\mathbf{V}_Z$ component is slightly stronger than the $\mathbf{V}_X$ and $\mathbf{V}_Y$ components, while the $\mathbf{R}_Z$ component is slightly weaker than the $\mathbf{R}_X$ and $\mathbf{R}_Y$ components. This suggests that the rotational motions for **E**2 are predominantly in horizontal directions, and the site effect is relatively weaker. In addition, the amplitude difference between the actual observed

https://doi.org/10.5194/npg-2024-17
Preprint. Discussion started: 24 July 2024

rotational and translational components is smaller than the amplitude difference between the simulated advective and rotational components, and the observed rotational component is relatively stronger, which is the same as the characteristic shown in Fig. 9. That is consistent with previous studies that have argued that the observed rotational components have a relatively stronger amplitude than the rotational component converted from translational components (Teisseyre et al., 2003).

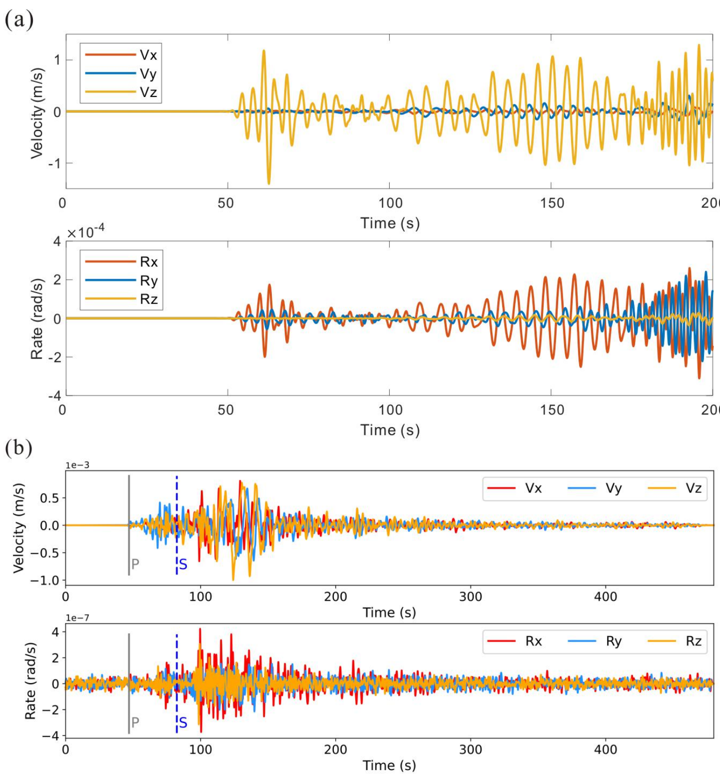

Figure 9. 6C seismic records of (a) theoretical simulation under linear small deformation for **E2**. In (b), for the real seismic records, a band-pass filter of 0.1 Hz to 1 Hz is applied, and the corresponding arrival times of P and S waves are calculated

https://doi.org/10.5194/npg-2024-17
Preprint. Discussion started: 24 July 2024

according to the iasp91 model (Kennett and Engdahl, 1991)

Following the numerical simulation of **E**1 and **E**2 under the conditions of linear and nonlinear simulations, respectively, we make a theoretical comparison by calculating the relative differences between the two scenarios. The relative changes in root-mean-square (RMS) amplitude are used to compare the linear errors of these two earthquakes. The RMS amplitude values of the waveforms recorded in a 2-s time window are calculated at 1-s intervals to reflect the energy of the seismic recordings, and then the relative change percentage of RMS amplitude of the nonlinear simulation results relative to that of the linear simulation is derived accordingly, and the results are shown in Fig. 10.

In Fig. 10a, it can be seen that the error of the nonlinear simulation of **E**1 is very small relative to the linear simulation, and only the error on the $\mathbf{V}_X$ component is slightly larger but is less than 0.4 %. This indicates that for the simulation of **E**1, the error introduced by the linear approximation is basically negligible. For the results of **E**2 in Fig. 10b, the translational components show larger errors than the rotational components, especially the $\mathbf{V}_X$ and $\mathbf{V}_Y$ components, with errors up to 10 %, and the errors on the $\mathbf{V}_Z$ components are basically within 5 %; the linear approximation errors on the three rotational components are even smaller, basically within 2 %. For the body waves dominated records before 120 s, $\mathbf{R}_X$ and $\mathbf{R}_Y$ components reflect a larger error percentage than $\mathbf{R}_Z$ component. In the surface-wave records after the 150 s, the $\mathbf{R}_Z$ component shows increased nonlinear errors. These results indicate that the linear simplification of rotation for the elastomer strain process has a small error for the

https://doi.org/10.5194/npg-2024-17
Preprint. Discussion started: 24 July 2024

rotational component but produces a larger wavefield error on the translational components.

The linear approximation produces more errors on the translational components obtained from real earthquake simulations, probably because the wavefield energy of rotational component decays faster in natural earthquakes (Lee et al., 2009; Lai and Sun, 2017). Besides, the simulation results of **E**2 show a larger difference between linearity and nonlinearity than that of **E**1, which is about ten times larger, mainly because of the increased source energy of **E**2. So, for weak and moderate earthquakes, the effect of nonlinearity may be negligible, and the linear approximation can meet the research accuracy. It can also be attributed to the fact that the two earthquakes have different source mechanisms, which makes its linear approximation error larger.

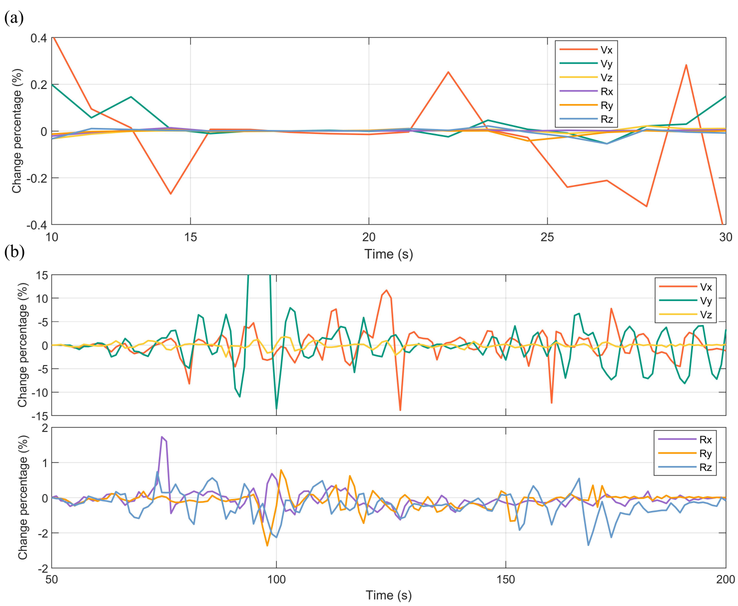

Figure 10. Relative changes in RMS amplitude of simulation results between linear and nonlinear scenarios for **E**1 (a) and **E**2 (b)

https://doi.org/10.5194/npg-2024-17
Preprint. Discussion started: 24 July 2024

5 Discussions

Compared with the traditional theory of seismic wave propagation in homogeneous elastic media, the Green strain tensor is a function of both the strain tensor and the rotation tensor, as shown in Eq. (5). Without considering the linear approximation of small deformation, the wave propagation equations entail three-order differentiations of displacement, with the higher-order terms influenced by shear modulus and bulk modulus. Given that earthquakes mostly occur in shallow crust or transitional zones between shell and mantle, often considered as planes of elastic attributes transformation and stress discontinuity zones, more intricate media and focal physics (Olson and Apsel, 1982; Olson and Allen, 2005), such as the model featuring a rigid thin-layer sphere (Zhu, 1983), warrant further exploration and discussion.

The mechanics of seismic rotation may be related to various factors, including nonlinear elasticity (Guyer and McCall, 1995; Guyer and Johnson, 1999), asymmetric moment tensor (Teisseyre et al., 2003; Teisseyre, 2010), medium heterogeneity, anisotropy (Pham et al., 2010; Sun et al., 2021), and site effects. This study focuses only on isotropic and homogeneous media and three fundamental moment tensor sources in the simulations of nonlinear small deformation. Therefore, the effect of nonlinear geometric relation on wave propagation, especially for rotational components, necessitates further investigation by testing the slipping angle, the shear moment, the elastic parameters, and the anisotropy, among others. The current

https://doi.org/10.5194/npg-2024-17
Preprint. Discussion started: 24 July 2024

discussion concentrates on wave propagation and the characteristics of 6-component wavefields excited by three basic moment tensor sources to discuss the theoretical approximation stemming solely from the linear assumption of small deformation, with further analyses of other contributing factors slated for future research endeavors.

Observations and simulations of Taiwan Hualien earthquakes have verified the existence of rotational motions along the northeast fault, resulting in prominent Rayleigh-wave recordings and indicative of a vertical slipping mechanism in the earthquake rupture process. In addition, the observation of stronger $\mathbf{R}_Z$ component and two horizontal components suggests the presence of Love surface waves., signifying clear horizontal slipping and torsion. This finding, aligning with Yu et al.'s (1999) discovery, reveals the existence of horizontal rotational mechanisms within the seismic belt of Taiwan attributed to the Pacific Plate beneath the Eurasian Plate from the east, coupled with northward pressure exerted by the Philippines Sea Plate.

The simulations show the nonlinear effect cannot be neglected for near, regional, and strong earthquakes, and that the rotational components observed at ground surface will be stronger than the theoretical one, consistent with previous research. Simulations in this study only portray the sources and medium in a simplified way. The simulations of real earthquake scenarios present a much more intricate interplay of source mechanisms and propagation mediums, encompassing long propagation distances, and long time scales. So, the simulations of observed earthquakes, especially for strong earthquakes, the nonlinear attributes through which seismic waves couple with each other amplify the discrepancies arising from the nonlinear

https://doi.org/10.5194/npg-2024-17
Preprint. Discussion started: 24 July 2024

assumption.

6 Conclusions

Based on seismic wave equations assuming linear small deformation, we have derived elastic-wave equations that incorporate nonlinear part of Green strain tensor. By numerical simulations in a three-dimensional full-space homogeneous medium model using the finite difference method, our study discusses the distinctive characteristics of translational and rotational motions elicited by three fundamental moment tensor sources, shedding light on the wavefield differences between linear and nonlinear assumptions. The following conclusions can be drawn from our study.

(1) Under the influence of the nonlinear Green tensor, the relative displacement, deformation, and strain of spatial mass element in response to external forces are superimposed with nonlinear second-order terms of strain tensor and rotation tensor, resulting in third-order terms of displacement related to the shear and bulk moduli in the propagation of elastic waves.

(2) Nonlinearity has a greater effect on ISO and CLVD sources than on DC sources, and the effect of nonlinearity on the wavefield energy increases exponentially with increasing magnitude. The nonlinear effect for ISO source primarily impacts S waves. CLVD source generates wavefield difference ranging from 10 % to 20 % in the 45° diagonal direction of P-wave front, similar to the anomalies caused by media anisotropy.

(3) The errors caused by linearity approximation in rotations are more

https://doi.org/10.5194/npg-2024-17
Preprint. Discussion started: 24 July 2024

Nonlinear Processes in Geophysics
Discussions

pronounced in pure basic seismic sources. Strong seismic events render the nonlinear effect unbearable in simulations, underscoring the necessity of considering nonlinear effects. In other cases, the linear approximation meets the accuracy requirements, so the linear approximation can be used for relevant questions. Nonlinear small deformation can be a factor in the rotational motion produced by strong earthquakes.

(4) The simulation of **E**1 and **E**2 primarily feature Rayleigh waves in vertical translation and horizontal rotation. However, actual observations indicate a prevalent existence of Love waves, potentially attributable to site effects or more complicated focal mechanisms. The stronger-energy **E**2 triggered relatively strong Love waves, so its error caused by the resulting nonlinearity is larger.

Author contributions. WL: conceptualization, methodology, investigation, formal analysis, writing - original draft. YW: conceptualization, writing - original draft and revised draft. CC: in vestigation, formal analysis. LS: methodology.

Data and resources. The seismic records of **E**1 are provided by the Institute of Earth Sciences, Academia Sinica, Taiwan, China. The translational records of **E**2 are acquired from the Fujian Earthquake Agency.

Competing interests. The contact author has declared that neither of the authors has any competing interes.

Disclaimer. Publisher's note: Copernicus Publications remains neutral with regard to jurisdictional claims made in the text, published maps, institutional affiliations, or any other geographical representation in this paper.

Financial support. This research is financially supported by the National Natural Science Foundation of China (No. 42150201、No. 62127815、No. U1839208).

References

Abercrombie, R. E.: Near-surface attenuation and site effects from comparison of surface and deep borehole recordings, Bull. Seismol. Soc. Am., 87 (3),731~744, https://doi.org/10.1029/96JB03485, 1997.

Aki, K., and P. G. Richards. Quantitative seismology, 2nd ed, California: University Science Books, https://doi.org/10.1029/2003EO210008, 2002.

Bataille, K., Contreras, M.: Nonlinear elastic effects on permanent deformation due to large earthquakes, Phys. Earth Planet. Inter., 175(1), 47-52, https://doi.org/10.1016/j.pepi.2008.02.016, 2009.

Bernauer, F., Wassermann, J., Guattari, F., Frenois, A., Bigueur, A., Gaillot, A., de Toldi, E., Ponceau, D., Schreiber, U., and Igel, H.: BlueSeis3A: Full characterization of a 3C broadband rotational seismometer, Seismol. Res. Lett., 89(2A), 620–629, https://doi.org/10.1785/0220170143, 2018.

Bernauer, M., Fichtner, A., and Igel, H.: Reducing nonuniqueness in finite source inversion using rotational ground motions, J. Geophys. Res.-Solid Earth, 119(6), 4860-4875, https://doi.org/10.1002/2014JB011042, 2014.

https://doi.org/10.5194/npg-2024-17
Preprint. Discussion started: 24 July 2024

Nonlinear Processes in Geophysics
Discussions

Cao, Y. W., Chen, Y. J., Zhou, T., Yang, C. X., Zhu, L. X., Zhang, D. F., Cao, Y. J., Zeng, W. Y., He, D., and Li, Z. B.: The development of a new IFOG-based 3C rotational seismometer, Sensors, 21(11), 3899, https://doi.org/10.3390/s21113899, 2021.

Chen, Q. J., Yin, J. E., and Yang, Y. S.: Time-frequency characteristic analysis of six-degree-freedom ground motion records, Chinese Quarterly of Mechanics, 35, (3), 499-506, https://doi.org/10.15959/j.cnki.0254-0053.2014.03.033, 2014.

Dong, L. G., and Ma, Z. T.: A staggered-grid high-order difference method of one-order elastic wave equation, Chinese J. Geophys., 43(3), 411-419, 2000 (in Chinese).

Donner, S., Bernauer, M., and Igel, H.: Inversion for seismic moment tensors combining translational and rotational ground motions, Geophys. J. Int., 207(1), 562-570, https://doi.org/10.1093/gji/ggw298, 2016.

Feng, X., Fehler, M., Brown, S., Szabo, T. L., and Burns, D.: Short-period nonlinear viscoelastic memory of rocks revealed by copropagating longitudinal acoustic waves, J. Geophys. Res.-Solid Earth, 123(5), 3993–4006, https://doi.org/10.1029/2017JB015012, 2018.

Graizer, V. M.: Strong motion recordings and residual displacements: what are we actually recording in strong motion seismology? Seismol. Res. Lett., 8(4), 635-639, https://doi.org/10.1785/gssrl.81.4.635, 2010.

Graves, R. W.: Simulating seismic wave propagation in 3D elastic media using staggered-frid finite differences, Bull. Seismol. Soc. Am., 86(4), 1091-1106,

https://doi.org/10.5194/npg-2024-17
Preprint. Discussion started: 24 July 2024

Nonlinear Processes in Geophysics
Discussions
Open Access
EGU

1996.

Grayzer, V. M.: Inertial seismometry methods, Earth Physics, 27(1), 51-61, 1991.

Guatteri, M., Spudich, P., and Beroza, G. C.: Inferring rate and state friction parameters from a rupture model of the 1995 Hyogo-ken Nanbu (Kobe) Japan earthquake, J. Geophys. Res.-Solid Earth, 106(B11), 26511-26521, https://doi.org/10.1029/2001JB000294, 2001.

Guyer, R. A., and McCall, K. P.: Hysteresis, discrete memory, and nonlinear wave propagation in rock: A new paradigm, Phys. Rev. Lett., 74(17), 3491-3495, https://doi.org/10.1103/physrevlett.74.3491, 1995.

Guyer, R. A., and Johnson, P. A.: Nonlinear mesoscopic elasticity: evidence for a new class of materials, Physics Today, 52(4), 30-36, https://doi.org/10.1063/1.882648, 1999.

Hua, S. B., and Zhang, Y.: Numerical experiments of moment tensor inversion with rotational ground motions, Chinese J. Geophys., 65(1), 197-213, https://doi.org/10.6038/cjg2022P0668, 2022.

Huras, L., Zembaty, Z., Bonkowski, P. A., and Bobraet, P.: Quantifying local stiffness loss in beams using rotation rate sensors, Mech. Syst. Signal Proc., 151, 107396, https://doi.org/10.1016/j.ymssp.2020.107396, 2021.

Ichinose, G. A., Ford, S. R., and Mellors, R. J.: Regional moment tensor inversion using rotational observations, J. Geophys. Res.-Solid Earth, 126(2), e2020JB020827, https://doi.org/10.1029/2020JB020827, 2021.

Jia, L., Yan, S. G., Zhang, B. X., and Huang, J.: Research on perturbation method for nonlinear elastic waves, J. Acoust. Soc. Am., 148, EL289–EL294, https://doi.org/10.1121/10.0001980, 2020.

Kennett, B. L. N., and Engdahl, E. R.: Traveltimes for global earthquake location and phase identification, Geophys. J. Int., 105(2), 429–465, https://doi.org/10.1111/j.1365-246X.1991.tb06724.x, 1991.

Knopoff, L., and Randall M. J.: The compensated linear-vector dipole: A possible mechanism for deep earthquakes, J. Geophy. Res., 75(26), 4957–4963, https://doi.org/10.1029/JB075i026p04957, 1970.

Kozak, J. T.: Tutorial on earthquake rotational effects: historical examples, Bull. Seismol. Soc. Am., 99(2B), 998-1010, https://doi.org/10.1785/0120080308, 2009.

Lai, X. L., and Sun, Y.: Three component rotational ground motion obtained from explosive source data, Earth science, 42(4), 645—651, 2017 (in Chinese).

Laske, G., Masters, G., Ma, Z. T., and Pasyanos, M.: Update on CRUST1. 0-A 1-degree global model of Earth's crust, EGU General Assembly 2013, 15, EGU2013-2658, 2013.

Lee, K. H. W., Igel, H., and Trifunac, D. M.: Recent Advances in Rotational Seismology, Seismol. Res. Lett., 80(3), 479-489, https://doi.org/10.1785/GSSRL.80.3.479, 2009.

Li, H. N.: Study on rotational components of ground motion, Journal of Shenyang Architectural and Civil Engineering Institute, 7(1), 88-93, 1991 (in Chinese).

Li, H. N., and Sun, L. Y.: Rotational components of earthquake ground motions derived from surface waves, Earthq. Eng. Eng. Vib., 21(1), 15-23, https://doi.org/10.13197/j.eeev.2001.01.003, 2001 (in Chinese).

Madariaga, R.: Dynamics of an expanding circular fault, Bull. Seismol. Soc. Am., 66(3), 639-666, https://doi.org/10.1007/BF02246368, 1976.

McCall, K. R.: Theoretical study of nonlinear elastic wave propagation, J. Geophys. Res., 99(B2), 2591-2600, https://doi.org/10.1029/93JB02974, 1994.

Oliveira, C. S., and Bolt, B. A.: Rotational components of surface strong ground motion. Earthq. Eng. Struct. D. 18(4), 517–526, https://doi.org/10.1002/eqe.4290180406, 1989.

Olson, A. H., and Apsel, R. J.: Finite faults and inverse theory with applications to the 1979 Imperial Valley earthquake, Bull. Seismol. Soc. Am., 72(6A), 1969-2001, https://doi.org/10.1785/BSSA07206A1969, 1982.

Olson, E. L., and Allen, R. M.: The deterministic nature of earthquake rupture, Nature, 438(7065), 212-215, https://doi.org/10.1038/nature04214, 2005.

Pham, N. D., Igel, H., Puente, J. D. L., Käser, M., and Schoenberg, M. A.: Rotational motions in homogeneous anisotropic elastic media. Geophysics 75(55), D47-D56, https://doi.org/10.1190/1.3479489, 2010.

Renaud, G., Le Bas, P. Y., and Johnson, P. A.: Revealing highly complex elastic nonlinear (anelastic) behavior of Earth materials applying a new probe: Dynamic acoustoelastic testing. J, Geophys. Res.-Solid Earth, 117, B06202, , https://doi.org/10.1029/2011JB009127, 2012.

https://doi.org/10.5194/npg-2024-17
Preprint. Discussion started: 24 July 2024

Renaud, G., Rivière, J., Le Bas, P. Y., and Johnson, P. A.: Hysteretic nonlinear elasticity of Berea sandstone at low-vibrational strain revealed by dynamic acoustoelastic testing, Geophys. Res. Lett., 40(4), 715-719, https://doi.org/10.1002/grl.50150, 2013.

Sun, L., Yu, Y., Lin, J. Q., and Liu, J. L.: Study on seismic rotation effect of simply supported skew girder bridge, Earthquake Engineering and Engineering Dynamics, 37(4), 121-128, https://doi.org/10.13197/j.eeev.2017.04.121.sunl.014, 2017 (in Chinese).

Sun, L. X., Wang, Y., Li, W., and Wei, Y. X.: The characteristics of seismic rotations in VTI medium, Appl. Sci.-Basel, 11(22), 10845, https://doi.org/10.3390/app112210845, 2021.

Sun, L. X., Zhang, Z., and Wang, Y.: Six-component elastic-wave simulation and analysis, EGU General Assembly 2018, Geophysical Research Abstracts, 20, EGU2018-14930-1, 2018.

Teisseyre, R.: Tutorial on new developments in the physics of rotational motions, Translated World Seismology, 99(2A), 1028-1039, https://doi.org/10.1785/0120080089, 2010.

Teisseyre, R., Suchcicki, J., Teisseyre, K. P., Wiszniowski J., and Palangio, P.: Seismic rotation waves: Basic elements of the theory and recordings, Annals of Geophysics, 46(4), 671–685, https://doi.org/10.4401/ag-4375, 2003.

TenCate, J. A., Malcolm, A. E., Feng, X., and Fehler, M. C.: The effect of crack orientation on the nonlinear interaction of a P wave with an S wave, Geophys. Res. Lett., 43(12), 6146-6152, https://doi.org/10.1002/2016GL069219, 2016.

https://doi.org/10.5194/npg-2024-17
Preprint. Discussion started: 24 July 2024

Nonlinear Processes in Geophysics
Discussions
Open Access

Wang, L., Luo, Y. H., and Xu, Y. H.: Numerical investigation of Rayleigh-wave propagation on topography surface, J. Appl. Geophys., 86, 88–97, https://doi.org/10.1016/j.jappgeo.2012.08.001, 2012.

Wang, X. S., and Lv, J.: The holistic clockwise rotation possibly existed in Taiwan region - in addition on the seismicity feature and earthquake prediction in its adjacent areas, South China Journal of Seismology, 2, 48-54, 2006 (in Chinese).

Wessel, P., Luis, J. F., Uieda, L., Scharroo, R., Wobbe, F., Smith, W. H. F., and Tian, D.: The generic mapping tools version 6, Geochemistry, Geophysics, Geosystems, 20, 5556–5564, https://doi.org/10.1029/2019GC008515, 2019.

Xu, Y. X., Xia, J. H., and Miller, R. D.: Numerical investigation of implementation of airearth boundary by acoustic-elastic boundary approach, Geophysics, 72 (5), SM147–SM153, https://doi.org/10.1190/1.2753831, 2007.

Yan, Y. Y.: Seismic response analysis of high-rise building under different types of multi-dimensional earthquake ground motions (Ph.D. dissertation), Jiangsu University, 2017(in Chinese).

Yu, S. B., Kuo, L. C., and Punongbayan, R. S., Emmanuel, G.R.: GPS observation of crustal deformation in Taiwan-Luzon region, Geophys. Res. Lett., 26(7), 923-926, https://doi.org/10.1029/1999GL900148, 1999.

Yuan, S. H., Simonelli, A., Lin, C. J., Bernauer, F., Donner, S., Braun, T., Wassermann, J., and Igel, H.: Six degree-of-freedom broadband ground-motion observations with portable sensors: Validation, local earthquakes, and signal processing, Bull. Seismol. Soc. Am., 110(3), 953–969, https://doi.org/10.1785/0120190277, 2020.

Yang, D.H., Liu, E., Zhang, Z.J., and Teng, J.: Finite-difference modelling in two-dimensional anisotropic media using a flux-corrected transport technique, Geophys. J. Int., 148(2), 320–328, https://doi.org/10.1046/j.0956-540x.2001.01575.x, 2002.

Zhao, K. C., and Zhang, X. B.: Distinguishing underground nuclear test by matrix decomposition, Acta Scientiarum Naturalium Universitatis Pekinensis, 58(4), 609-614, https://doi.org/10.13209/j.0479-8023.2022.042, 2022 (in Chinese).

Zheng, H. S., Z. J. Zhang, and Liu, E. R.: Nonlinear seismic wave propagation in anisotropic media using the flux-corrected transport technique, Geophys. J. Int., 165(3), 943-956, https://doi.org/10.1111/j.1365-246X.2006.02966.x, 2006.

Zheng, X.,F., Cheng, Z.,H., and Zhang, C. H.: The development of seismic monitoring in Taiwan, Seismological and Geomagnetic Observation and Research, 26(3), 100-107, https://doi.org/10.3969/j.issn.1003-3246.2005.03.017, 2005 (in Chinese).

Zhou, C., Zeng, X. Z., Wang, Q. L., and Liu, W. Y., and Wang, C. Z.: Rotational motions of the Ms7.0 Jiuzhaigou earthquake with ground tilt data, Science China Earth Science, 62(5), 832-842, https://doi.org/10.1007/s11430-018-9320-3, 2019.

Zhu, Z. X.: On the nonlinear strain measures, Advances in Mechanics, 13(2), 259-272, 1983 (in Chinese).